
# TUC-TUC: Development of a test bench for the study of rotor aeroacoustics

Isaac Bensignor[1], Lourenco Tercio Lima Pereira, and Daniele Ragni
Faculty of Aerospace Engineering
Delft University of Technology
Kluyverweg 1
2629HS Delft
The Netherlands

**ABSTRACT**

*This work describes the development of a test bench that allows for a complete assessment of the aerodynamic characteristics and the acoustic emissions of a rotor in flight-like operating conditions. The rotor is named TUC-TUC, after the TU delft Characterization model for roTor aeroacoUstiCs. Its design is driven by the ability of precisely control its configuration and load distribution while facilitating a holistic set of aeroacoustic measurement techniques to take place. The design rationale, technical developments, experimental plans, estimated performance and noise emissions are shown in this study.*

## 1. INTRODUCTION

The regulatory process enabling beyond visual line of sight drone vehicles to operate autonomously or under remote piloting below 150 meters has been underway for years [1–3]. These vehicles execute rapid maneuvers while maintaining stable attitudes, speeds, and altitudes amid dynamic conditions such as gusts, turbulence, boundary layers, and environmental or operational changes. In urban settings, these challenges intensify due to the complex fluid flow environments created by dense clusters of buildings and natural structures. As a result, accurately estimating noise emissions in realistic flight scenarios becomes essential, as they are closely linked to the vehicles' operational dynamics. This need is further exacerbated by the accelerated development of Urban Aerial Transportation (UAT), which often conflicts with existing legislative efforts aimed at reducing community sound exposure. UAT vehicles typically rely on open rotors or propellers for lift and propulsion, and they are also the primary sources of noise emissions. Therefore, as the transportation landscape evolves, it is critical to consider the environmental impacts of these vehicles, particularly noise, alongside operational safety to ensure public acceptance and the long-term sustainability of this emerging field [4].

The theoretical foundations of rotor noise have been well established over the last half-century [5–7]. The rotation of blades is fundamentally responsible for the noise that is radiated, yielding a

[1]i.bensignor@tudelft.nl (corresponding author)

noise spectrum that contains tonal and broadband components. For tonal noise in particular, the peak frequencies excited are harmonic multiples of the blade passing frequency (BPF). The BPF is defined in Equation 1 as:

$$BPF = \frac{Bn}{60} \tag{1}$$

where $B$ is the number of blades rotating and $n$ is the rotational frequency in RPM. The tonal noise generated by rotating blades is a result of periodic mass displacement (i.e. thickness noise) and by aerodynamic forces (i.e. loading noise). For moderately to highly loaded propellers/rotors, the latter dominates the acoustic energy emitted.

Studying rotor noise presents significant challenges. Discrepancies frequently arise from the difficulty of reproducing the assumptions underlying theoretical models and the sensitivity of acoustic behavior to key parameters. A major contributor is the inability to maintain fully steady and symmetric flow conditions, along with the challenge of minimizing spurious noise from, for example, motors. These issues are compounded by limitations in current measurement techniques and the complex geometries of typical blade configurations, which hinder the acquisition of detailed flow data. As a result, some reported discrepancies in noise emissions exceed 10 dB, often lacking clearly identifiable causes [8]. Therefore, while both experimental and numerical studies on rotating bodies have been conducted extensively [9, 10], cross-validation remains difficult due to high uncertainties and sparse datasets.

Experimental data are often restricted to steady-state loads and torques at fixed rotational speeds. Measurements of the flow field surrounding or of the pressure over the blades have been achieved via Particle Image Velocimetry (PIV) or Pressure Sensitive Paint (PSP) techniques [11–13]. Nevertheless, these methods are still limited by the conditions measured in and the complexity of the flow and/or model geometry. Moreover, most experiments are still conducted in clean, controlled wind tunnel environments that do not reflect the dynamic, time-varying conditions experienced in free flight. Consequently, the resulting acoustic signatures may not represent real-world urban environments, and the rotor's response to unsteady flow remains poorly understood. These limitations raise an important question: how can regulators define acceptable noise thresholds for UAT if current testing environments fail to reflect operational reality?

This work aims to close the gap in rotor noise characterization by developing detailed experimental studies that assess aeroacoustic emissions for realistic and representative flow conditions of UAT vehicles. Using a dedicated acoustic test bench and novel experimental techniques, the study addresses the challenges posed by the complex geometry of rotors, their associated unsteady flow fields, and the inherent difficulties of performing aerodynamic measurements on rotating bodies. These factors often hinder direct, physics-driven validation of rotor aeroacoustics, and mitigating these sources of uncertainty is a central objective. To achieve this, a characterization rotor, or propeller (used herein interchangeably), and accompanying experimental setup have been developed to enable a holistic assessment of noise emissions. At the core of this effort is TUC-TUC, the **TU** Delft **C**haracterization model for ro**T**or aeroaco**U**sti**C**s, which is a simplified rotor designed to improve the measurability of key aerodynamic phenomena linked to noise generation. The acoustic test bench approach allows for direct comparison of experimental data (i.e. far field microphone and PSP measurements) with theoretical and physics-based models. This work presents the design rationale of TUC-TUC, the supporting hardware for operating it, and discussion of how it will be tested. The following section details the driving design characteristics of TUC-TUC, including the geometry and the specific design considerations made. Afterwards is a discussion of how TUC-TUC's performance was estimated to reach the final design. Finally the experimental setup and methods are presented, along with a description of what conditions TUC-TUC will be tested in.

## 2. DRIVING DESIGN CHARACTERISTICS OF TUC-TUC

The design of TUC-TUC started with an assessment of general requirements for a rotor system

tailored to aeroacoustic investigations. The goal was to identify the essential features needed to test the basic aerodynamic and aeroacoustic characteristics of airfoils in rotating systems. A two bladed propeller is selected as a best compromise between minimum number of blades – allowing for the assessment of lower harmonics of the shaft frequency – and simplicity for balancing. Ideally, to test rotor aeroacoustics just a simple blade element rotating in space is desired as the test article. This ideal blade element is composed of a single airfoil section with no twist, taper, or sweep. Moreover, the element should be pitch controlled so blade loading, and hence loading noise, can be varied. To enable pitch control, a structure is required to rotate the airfoil. This led to the concept of a double-airfoil system on each half-span, with independent pitch control. The inner, smaller airfoil serves as the structural element that rotates the outer airfoil (the test article). A flat-plate divider is placed between the two airfoils to prevent the development of spanwise flow features. This plate serves a dual purpose: it minimizes aerodynamic interaction between the inner and outer sections and facilitates independent pitch control of the two sections. Additionally, the rotor includes a tip end plate, intended to reduce the formation of tip vortices and its associated noise. The key factors driving the design of TUC-TUC were:

1. The signal (outer blade section load and noise) to noise (inner airfoil load and noise) ratio estimated via velocity scaling laws [7],
2. The thickness of the airfoils so that the structure can withstand the high centrifugal loadings,
3. The expected dynamic pressure levels at the outer blade section, which would allow for lower uncertainty in aerodynamic measurements, possibly enabling the use of PSP,
4. Operating the rotor at speeds above the cutoff frequency of the available anechoic wind-tunnel testing facility ("A-Tunnel," detailed further in Section 3),
5. Not exceeding a rotor diameter of 0.4 m.

The efficiency of TUC-TUC in terms of thrust, torque or figure of merit is not relevant to the scope of this research effort (however, they are estimated and measured). Additionally, use of classical efficiency increasing design features, like twisted, cambered airfoils with an optimized planform and tip shape, is purposefully not used as these features' impact cannot easily be decomposed from the overall aerodynamic and acoustic response to be measured. Modularity was a core design principle of the new system, thus TUC-TUC can easily swap its component to test other airfoils. This feature allows for a broad and adjustable testing infrastructure for current and future investigations.

## 3. GEOMETRY AND DESIGN SPECIFICATIONS

The design of TUC TUC was made in collaboration with the Electrical and Mechanical Development Department (DEMO) at TU Delft. The final rotor is shown in Figs. 1a and 1b. A comprehensive list of estimated and assumed operational conditions are presented in Table 1, which served to drive the design. The design chord based Reynolds number (Re) and Mach numbers (M) are also shown. The TU Delft Anechoic Wind Tunnel (A-Tunnel), has a cut-off acoustic frequency of 200 Hz, which leads to a minimum rotational speed of 6,000 RPM to ensure BPFs exceeds the anechoic chamber cutoff. The maximum allowable rotor radius for tests in this facility is determined to 0.2 m, following the tunnel nozzle radius of 0.3 m [14].

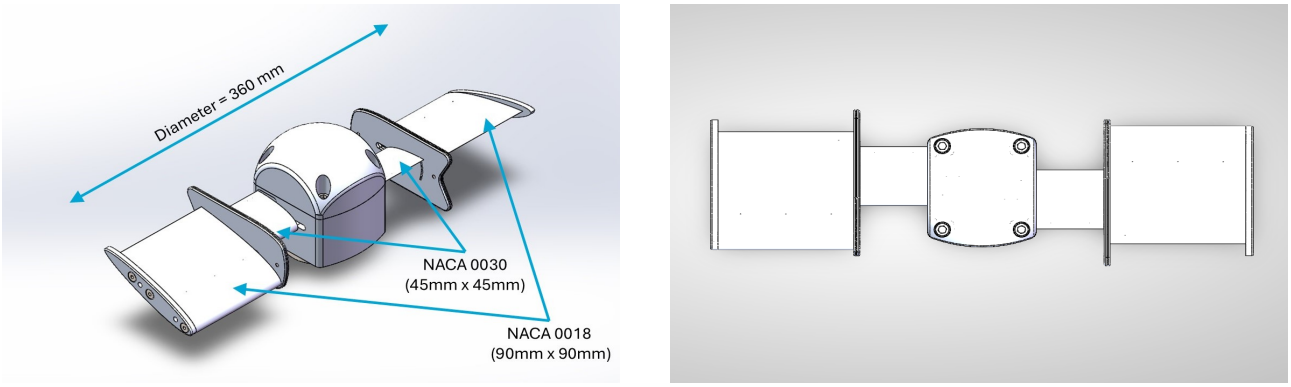


(a) (b)

Figure 1: (a) TUC-TUC system, designed for studying isolated rotor airfoil aeroacoustic characteristics. Trimetric view with key component dimensions shown. (b) TUC-TUC system, top view.

Table 1: **Design Test Conditions**

| | | |
|---|---|---|
| Rot. Speed | 6,000 | RPM |
| $\Omega$, Rot. Speed | 628 | Rad/s |
| $V$, Tip Velocity | 113 | m/s |
| Re, Outboard Airfoil Mid-span | 484,000 | |
| M, Outboard Airfoil Mid-span | 0.24 | |
| Tip Mach Number | 0.33 | |
| Re, Inboard Airfoil Mid-span | 109,000 | |
| M, Inboard Airfoil Mid-span | 0.11 | |
| Tip Outer Section Dyn. Pres. | 7,600 | Pa |
| Root Outer Section Dyn. Pres. | 1,700 | Pa |

Due to the high centrifugal loading of the rotor along the spar and mass balancing concerns determined via extensive FEA analysis, the spar was placed on the 52% chord position for the outer airfoil. For the inner airfoil, the spar passes through the 30% chord location (near to its max. thickness location). A central bolt with a 20 $N\ m$ pre-tension is used to secure the blade sections in place. The inner airfoil of TUC-TUC is a NACA 0030 and the outer airfoil is a NACA 0018. Both airfoils are untwisted, constant chord, and have aspect ratios equaling one. Moreover, X-Foil simulations of each airfoil at the design testing condition (inner airfoil angle fixed at zero degrees, outer airfoil angle varying) showed no indication of separation. This check ensured that the baseline condition did not inherently represent a high torque and noise scenario. Further rotor component details are listed in Table 2.

Based on the velocity scaling laws detailed in Hubbard *et al.* [7], the estimated signal-to-noise ratio (SNR) between the outer and inner sections of the TUC-TUC system is 27 and 18 dB when a $V^6$ (dipole) and $V^4$ (monopole) acoustic power scaling dependence assumption is made, respectively. The velocity at each airfoil's half span location is used in the calculation. For the $V^6$ scaling, the airfoil planform area is used (chord times span). For the $V^4$ scaling, the airfoil frontal projected area is used (max. airfoil thickness times span). These proportionalities are shown in Eqs. 2 and 3, respectively.

Table 2: **TUC-TUC Characteristics**

| | | | | | |
|---|---|---|---|---|---|
| (Inboard) NACA 0030 Chord | 45.0 | mm | Hub Radius | 36.0 | mm |
| Mid. Plate Chord | 105.0 | mm | Tip Radius | 180.0 | mm |
| Mid. Plate Span Width | 4.0 | mm | Number of "blades" | 2 | |
| Mid. Plate Max. Thickness | 54.0 | mm | Solidity, $\sigma = \frac{A_{Blades}}{A_{Disk}}$ | 0.216 | |
| (Outboard) NACA 0018 Chord | 90.0 | mm | Rotor Head Total Mass | 1.34 | kg |
| Tip Plate Chord | 99.0 | mm | | | |
| Tip Plate Span Width | 5.0 | mm | | | |
| Tip Plate Max. Thickness | 17.8 | mm | | | |

$$SNR \propto 10 * log_{10} \frac{[A_{planf.} * V^6]_{NACA\ 0018}}{[A_{planf.} * V^6]_{NACA\ 0030}} \tag{2}$$

$$SNR \propto 10 * log_{10} \frac{[A_{proj.} * V^4]_{NACA\ 0018}}{[A_{proj.} * V^4]_{NACA\ 0030}} \tag{3}$$

The flat plate in between the airfoils and the tip plate were designed with inspiration from Wadlin *et al.'s* [15] NACA Report on the effects of end plates on hydrofoil characteristics. The mid. flat plate chord is 1.16 times the outboard airfoil chord and its height (max. thickness) is 3.33 times the outboard airfoil max. thickness. The plate possess filleted edges and a fish tail like trailing edge. The elliptical tip flat plate is 1.1 times the outboard airfoil chord length and has a max. thickness of 1.1 times the max. outboard airfoil thickness. The leading edge of the tip plate has the same curvature as the leading edge of the outboard airfoil.

The independent angle of attack mechanism is unique to this rotor setup and requires manual intervention each time a new angle or flow speed is to be tested. Figures 2a, 2b and 3 show views of the angle setting mechanism. The outboard airfoil has a pitch mechanism resolution of two degree, and the inboard airfoil has a 2.5 degree resolution. Both airfoils are set via a pin/hole reference pattern. Due to the angle resolution necessary for the pin/hole pattern arc, interchangeable plates are used for achieving the entire angle setting range of $\pm 20^o$. Figure 3 also shows a slot on the middle flat plate where instrumentation wires originating in the hub can pass through. The outboard airfoils also possess three 0.2 mm diameter holes evenly distributed on both the suction and pressure side at the 1/3 chord.

(a) (b)

Figure 2: Spanwise axis views of: (a) TUC TUC middle flat plate and outboard airfoil. Arc hole resolution for setting the pitch is two degrees. Airfoil is pitched at -20 degrees. (b) TUC TUC tip flat plate and outboard airfoil.

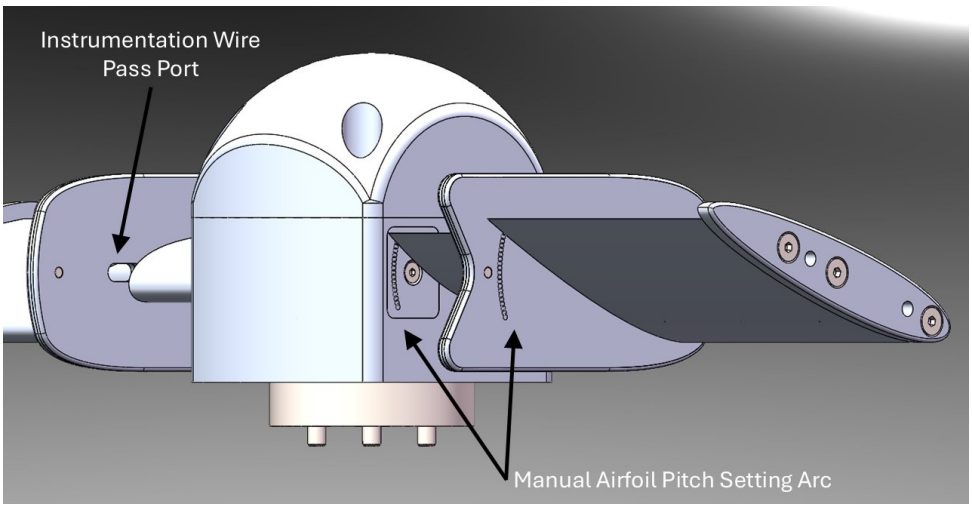


Figure 3: TUC TUC system, showing the independent pitch setting mechanism, and spanwise wire pass through ports.

## 4. PERFORMANCE ESTIMATIONS

TUC-TUC's performance is estimated using an in-house developed Blade Element Momentum Theory (BEMT) model. This study employs Leishman's BEMT implementation [16] for multiple purposes: initial sizing and design of TUC-TUC; estimating performance across various flight conditions; supporting future cross-validation of thrust and torque load cell measurements; and assessing tonal far-field acoustics through integration with Hanson's model [5] and comparison to microphone data. As a reduced-fidelity model BEMT offers rapid performance estimation capabilities compared to high-fidelity CFD simulations of rotor noise. BEMT is an efficient and valuable tool for preliminary rotor performance and (tonal) noise estimation.

Performance estimates are presented in Figure 4, where the geometric angle of attack ($\alpha$) variation is shown for the outer blade, and the inner blade angle is noted. Performance is shown in terms of the thrust and torque coefficients, which are defined by Eqs. 4 and 5, respectively. In the equations: $T$ is thrust (N), $Q$ is torque (N m), $\rho$ is the fluid density (kg/m$^3$), $A$ is the disk area (m$^2$), $\Omega$ is the rotational speed (rad/s), and $R$ is the tip radius (m). Equation 6 describes the advance ratio as the axial flow speed (m/s), $U_\infty$, normalized by the tip speed (m/s), $\Omega R_{tip}$. Two representative conditions are shown in Fig. 4: hover, $J = 0$, and an axial flow speed of 5 m/s, $J = 0.04$. Results are shown for rotational speeds of 3,000 and 6,000 RPM, which are equivalent to tip Reynolds numbers of 374,000 and 749,000 and tip Mach numbers of 0.17 and 0.33, respectively.

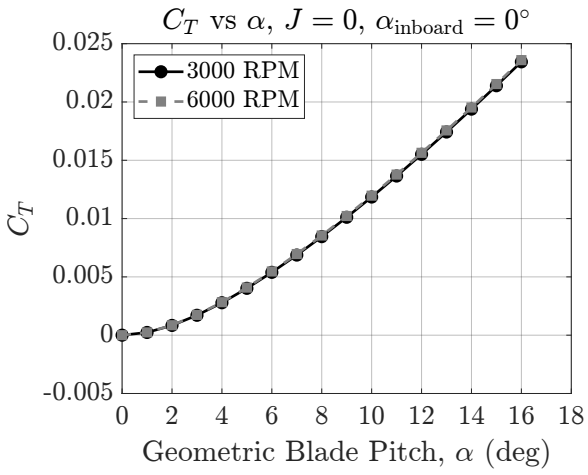


(a) $C_T$ vs. $\boldsymbol{\alpha}$ at $J = 0$

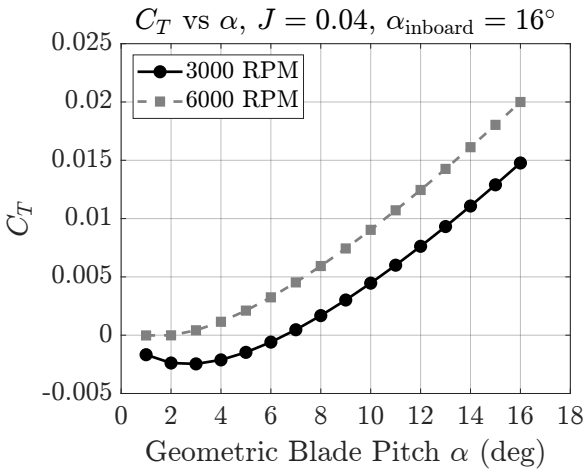


(b) $C_T$ vs. $\boldsymbol{\alpha}$ at $J = 0.04$

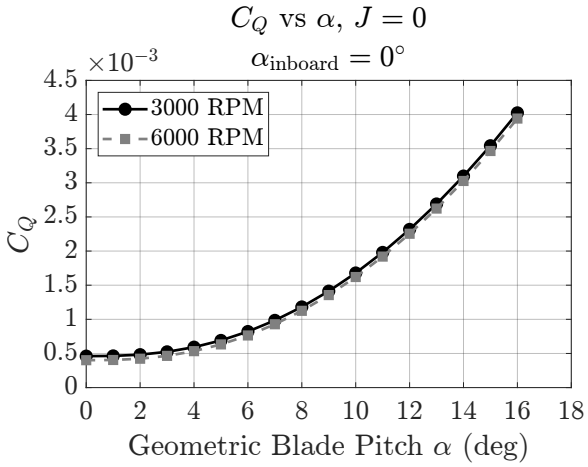


(c) $C_Q$ vs. $\boldsymbol{\alpha}$ at $J = 0$

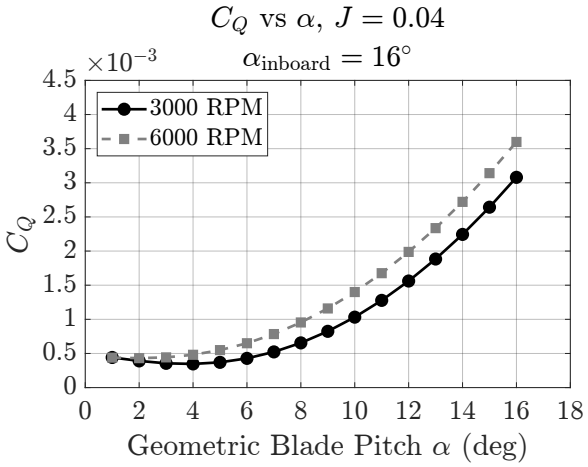


(d) $C_Q$ vs. $\boldsymbol{\alpha}$ at $J = 0.04$

Figure 4: Thrust and torque coefficients ($C_T$, $C_Q$) versus geometric angle of attack ($\alpha$) at advance ratios $J = 0$ and $J = 0.04$.

$$C_T = \frac{T}{\rho A \Omega^2 R^2}. \tag{4}$$

$$C_Q = \frac{Q}{\rho A \Omega^2 R^3}. \tag{5}$$

$$J = \frac{U_\infty}{\Omega R_{tip}} \tag{6}$$

The double airfoil span configuration enables selection of the inboard airfoil's geometric angle of attack such that the outboard airfoil's acoustic response can be quasi-isolated during testing. This is achieved by adjusting the inboard airfoil angle to minimize its aerodynamic loading, ideally yielding an effective angle of attack near zero degrees for a given flight condition. Using the BEMT model, for a range of advance ratios the optimum angle can be identified that determines the least intrusive inboard airfoil position. The objective across all conditions is to approach minimal effective angle of attack, where radiated noise is reduced. This relationship is expressed in Equation 7:

$$\alpha_{eff.} = \alpha_{geo.} - \frac{\lambda_{ind.}}{r} - \frac{\lambda_{ax.}}{r} \tag{7}$$

where $\alpha_{\text{eff.}}$ is the effective angle of attack, $\alpha_{\text{geo.}}$ is the geometric angle, $\lambda_{\text{ind.}}$ is the induced inflow angle, $\lambda_{\text{axial}}$ accounts for axial inflow due to free-stream velocity, and $r$ is the radial position

normalized by the tip radius. Figure 5 illustrates the dependence of optimal inboard angle of attack on inflow speed for representative flight conditions. The charts allow for the optimal setting of the inner blade section, such as to minimize its loading and contribution to noise.

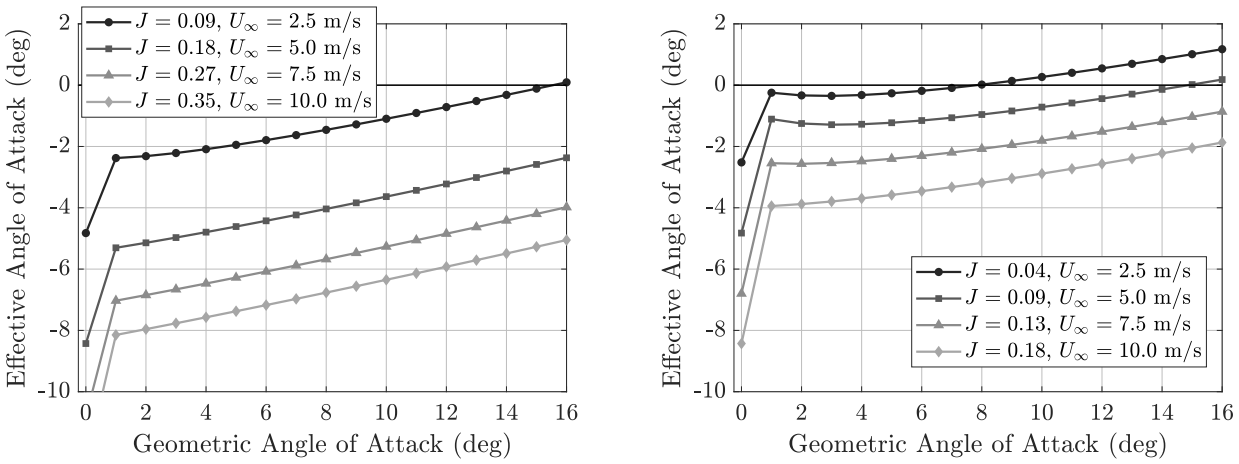


(a) RPM = 3,000

(b) RPM = 6,000

Figure 5: Geometric vs. effective angle of attack of the inner blade section for (a) RPM = 3,000 and (b) RPM = 6,000 under different advance ratio ($J$) conditions.

An estimate of the tonal noise emissions from the model's aerodynamic loading is carried out by assuming a series of rotating dipoles, following the predictions of the BEMT model. The estimations take into account the normal (thrust) and azimuthal (torque) force distribution along the blade. It is important to highlight that at this early stage no consideration is made for thickness noise. Figure 6 shows the obtained results at hover ($J = 0$) and 6,000 RPM. Other conditions are not displayed here for conciseness, which follow similar observed trends. Figure 6a demonstrates noise sound pressure level spectrum for varying outer blade pitch angles. Figures 6b and 6c show the noise directivity patterns predicted for the overall sound pressure levels. The former shows again how directivity is changed with the variation of outer blade pitch angle. The latter shows a decomposition of the noise emissions due to thrust and torque noise at outer airfoil $\alpha = 4°$. These noise estimates show that by changing the outer blade pitch the noise emissions can be modified. For $\alpha = 0°$ to $\alpha = 16°$, the steady loading noise changes by more than 10 dBs. This trend shows that loading noise increases with increasing blade pitch angle (i.e. increasing thrust and torque). The noise directivity patterns generally exhibit a two-lobe figure-eight pattern, which is dominated by thrust noise [17]. This is strictly not the case for $\alpha = 0°$, where the all zero degree angle of attack symmetry yields no thrust. However, the blade's dipolar-like acoustic response is dominated by torque noise as a result of the inherent profile drag. Figure 6c shows the decomposition of the noise directivity due to thrust and torque components. Here it can be observed the influence of torque noise, dominating the emissions along the rotor plane, and thrust noise, which dominates the noise emissions in the other directions.

The aerodynamic and aeroacoustic estimates presented provide preliminary insight into the forces and noise trends, the magnitude of the difference in response expected, and dominant flow and noise mechanisms to be observed during the experimental campaigns. Their simplicity do not allow for final conclusions. Nevertheless, these results serves as a guide for decision-making and verification of correct functioning of the bench model. The following sections, will explore the approach to experimenting with TUC-TUC.

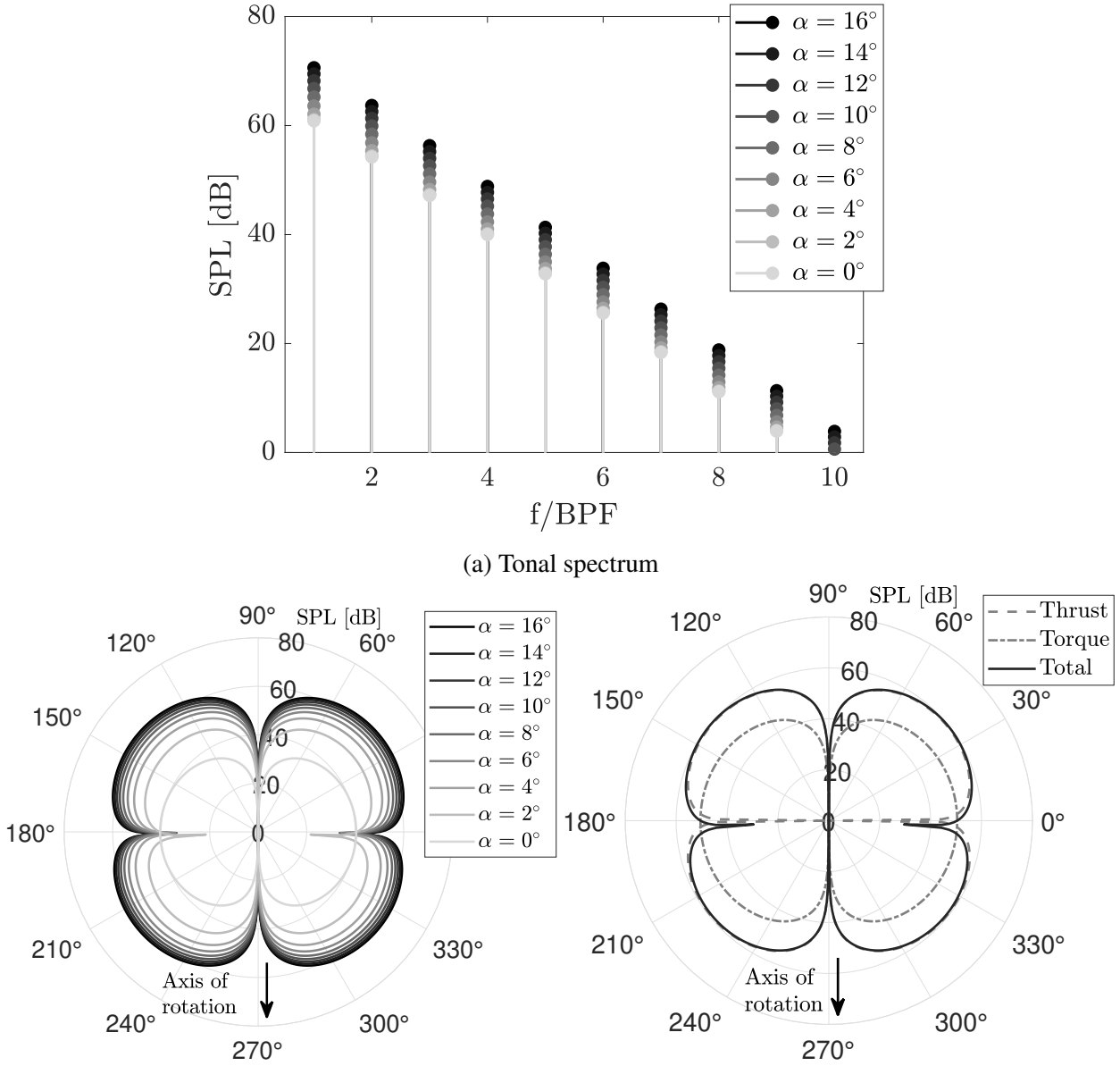


(a) Tonal spectrum

(b) Directivity pattern

(c) Decomposition of noise components at $\alpha$ = 4°

Figure 6: Estimations of tonal noise emissions from TUC-TUC at RPM = 6,000 and $J = 0$. Noise levels are estimated 10 m from the propeller axis.

## 5. EXPERIMENTAL HARDWARE, SETUP, AND METHODS

An experimental campaign with TUC-TUC is planned for June 2025. The main objectives of the campaign are to characterize the rotor, noise emissions and flow field over the blades in hover and axial steady flow conditions. The following sub-sections describe the experiment, setup, and method in further detail.

### 5.1. Flow Facility and Measurement Apparatus

Experiments are conducted in the A-Tunnel facility at TU Delft. This vertical open-test section anechoic wind tunnel can reach speeds of up to 35 m/s when using a circular nozzle of 600 mm diameter. Flow uniformity is demonstrated below 1% while turbulence intensities are well below 0.2%. The test section is surrounded by a semi-anechoic chamber with cut-off frequencies above 200 Hz. The facility is fully detailed in the work of Merino-Martinez *et al.* [14]. A microphone arc is placed parallel to the azimuthal axis of TUC-TUC. The arc comprises of 8 GRAS 46 BE microphones

installed at 1.0 m from the propeller axis. The directivity angles of the microphones vary from -20 to +60° in 10° steps. The microphone at 0° sits in the same horizontal plane of rotation as the propellor.

### 5.2. The "Rotor Rig"

TUC-TUC is installed to a rig dedicated for isolated propeller experiments. Figure 7a shows TUC-TUC installed on the nacelle support structure, and 7b highlights some of the load path components noted. Figure 8a shows the dynamic pitch system with the nacelle and propellor mounted and 8b shows a sectioned view removing one of two acoustically treated walls to see the rotating mechanism and wake rake.

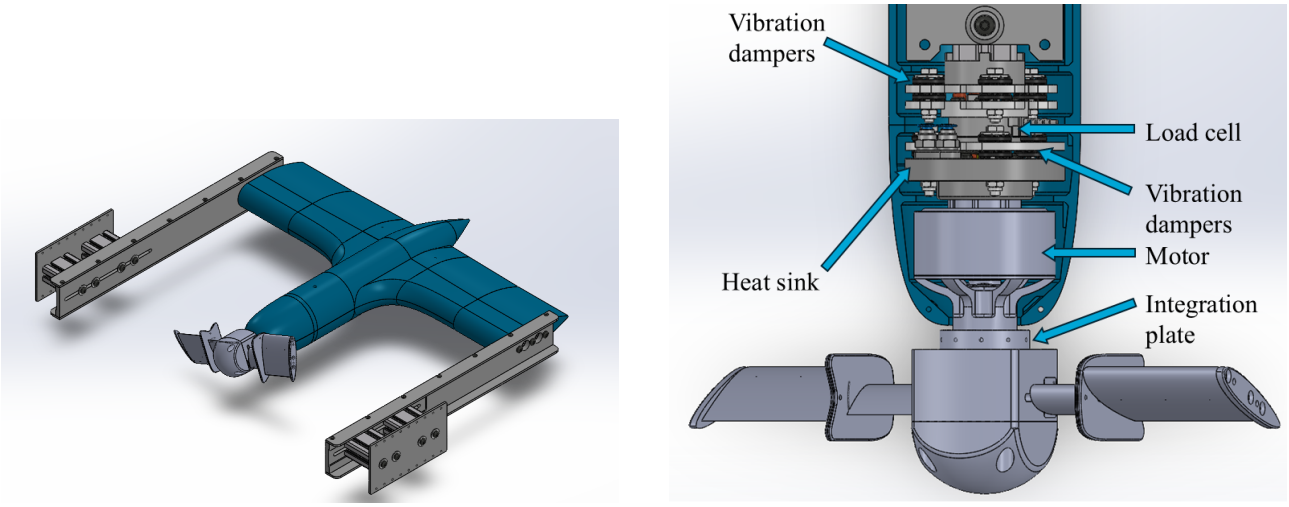


(a) Trimetric view of TUC-TUC mounted on supporting nacelle

(b) Annotated load path

Figure 7: Trimetric view and annotated load path view of the TUC-TUC rotor system.

A 7kW Hacker QSL-T-80-35-6 V2 motor is used for driving the rotor. Motor control is facilitated via a Silixcon 18 kW electronic speed controller. Because the motor is enclosed within a 3D-printed nacelle, prolonged operation can lead to elevated temperatures that may compromise measurement and control accuracy. To mitigate this, thermal management is provided by a custom 3D-printed metal heat sink with internal water-cooling channels connected to an external chiller. Temperature sensors and a magnetic encoder complement the motor system, allowing for internal temperature and RPM monitoring and control. Additionally, the encoder serves as a 1/revolution trigger signal for the illumination sources and cameras needed during PIV and PSP analysis.

Force and torque measurements are captured using a six axis ATI Mini45 load cell, calibrated for nominal loads of up to 580 N and torques of 10 N m along the axial and all torque axes, respectively. Rubber vibration dampers are placed between the heat sink plate and load cell, as well as between the load cell and rotor rig, to attenuate structural vibrations induced by unsteady propeller loading that could introduce spurious noise in the microphone measurements. The rotor rig is mounted on a dynamic pitch system so its orientation can be changed such that different side-slip angles can be assessed during wind-tunnel operation. A wake rake sits on a stepper motor controlled X-Y translation table on top of the system and allows for measurements of the downstream flow.

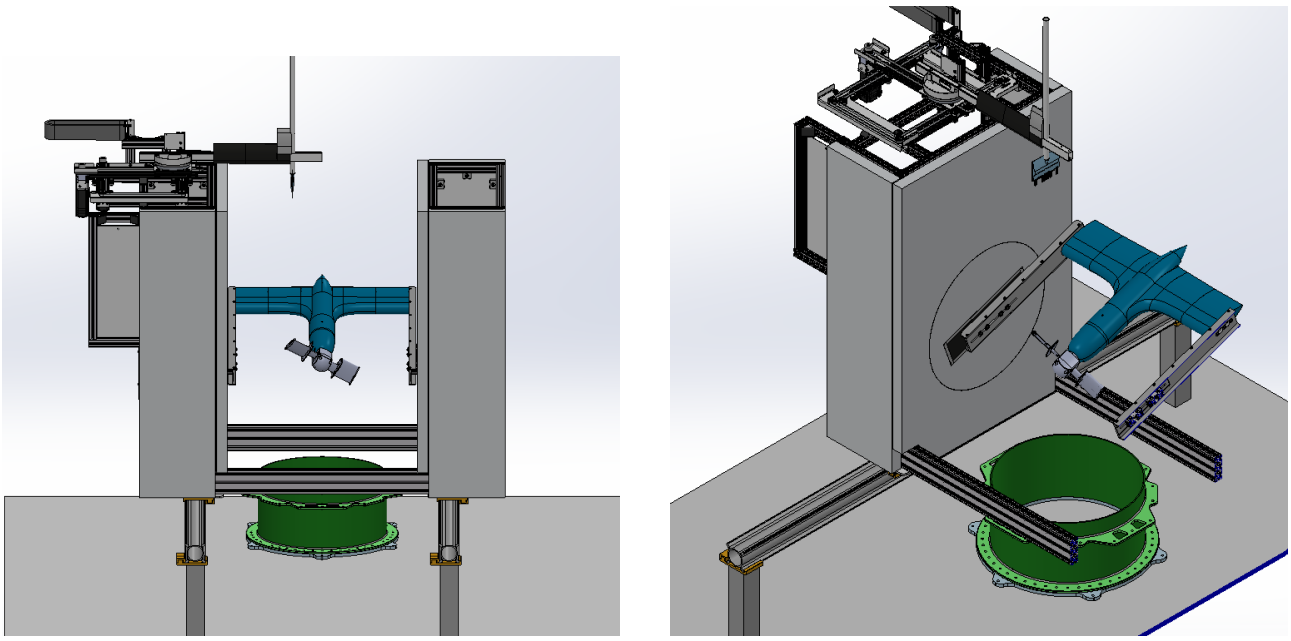

(a) Front view (b) Sectioned view

Figure 8: Front and sectioned view of the TUC-TUC rotor system.

### 5.3. Flow and Surface Measurement Techniques

To complement the acoustic and integral loads measurements, flow diagnostic techniques are also carried out. For that, two techniques are here explored, PIV and PSP. PIV is carried out over planes along the propeller outer blade. A planar, dual-pulse PIV setup is used [18], where two cameras are positioned such to cover both suction and pressure sides of the blade. Two Imager sCMOS LaVision cameras are used together with a Quantel Evergreen 200 mJ laser. LaVision Davis and timing unit are used for the synchronization and data acquisition. PSP measurements are performed for the propellor's outer airfoil suction and pressure sides. Two HardSoft IL-107 LEDs illuminate the PSP and the two aforementioned sCMOS cameras image the surface. Future works will detail the experimental results and conclusions from the techniques employed.

The outer blade section houses two thermocouples and four pressure sensors, each located in the vicinity of the model suction peak. This pressure sensor allows for both steady and unsteady pressure characterization. The temperature sensors occupy the two mid-holes. Sensor wiring is routed through the mid plate and inner airfoil to the hub, where a dedicated Raspberry Pi Pico 2W and battery are located. Temperature and pressure measurements are digitized using a 16-bit K-type thermocouple breakout and an Adafruit ADS1115 16-bit analog-to-digital converter, respectively. The data is transmitted live over WiFi and logged by a PC. The recorded data enables in-situ correction of PSP measurements during post-processing.

### 5.4. Test Conditions

Initial experiments assessing steady conditions in hover and non-zero advance ratios are to be carried out for the conditions shown in Table 3. The format presented indicates the start, increment, and end condition as [start:increment:end]. Moreover, an extended baseline characterization will test the rotor operating with only the inner airfoil and mid-plate for a representative subset of the conditions in Table 3. Measuring the acoustic response of this inner configuration will provide insight into its contribution relative to the noise generated by the entire system.

Table 3: Experimental Test Matrix

| RPM | $U_\infty$ range | Outer airfoil pitch angle |
|---|---|---|
| 2,000 | [0:10:20] | [-10:2:20] |
| 3,000 | [0:10:20] | [-10:2:20] |
| 4,000 | [0:10:20] | [-10:2:20] |
| 5,000 | [0:10:20] | [-10:2:20] |
| 6,000 | [0:10:20] | [-10:2:20] |

## 6. CONCLUSION

This work presents the development of a novel test article designed for the investigation of noise emissions from rotors. Central to this development is the creation of a model that enables a comprehensive assessment of the fundamental sources of rotor noise, namely, the distribution of aerodynamic forces over the blades resulting from the surrounding flow field.

The proposed design features an idealized two-bladed rotor comprising two distinct blade sections: an inner and an outer airfoil. The outer section is specifically designed to amplify noise-generating mechanisms, while the inner section is intended to minimize aerodynamic loading and, consequently, noise emissions. The inner section thus functions primarily as a structural support for the outer blade. This design strategy enhances the feasibility and accuracy of aeroacoustic measurements by concentrating noise generation in regions of higher dynamic pressure.

The rotor blades are intentionally simplified, consisting of symmetric, untapered, and untwisted airfoil sections. This configuration facilitates optical access, controlled experimental conditions, and a more integrated evaluation of both flow and acoustic phenomena. Furthermore, the pitch angles of the inner and outer blade sections can be independently adjusted. Under varying inflow conditions, the inner blade pitch is set to minimize its aerodynamic contribution, thereby isolating and enabling detailed study of the outer blade's aeroacoustic behavior across different pitch settings.

The rotor design is supported by preliminary performance and noise predictions, which indicate the expected trends in total aerodynamic loading and acoustic emissions. An experimental campaign is scheduled for June 2025, during which the rotor will undergo initial characterization. This will include acoustic and integral load measurements, followed by detailed flow field diagnostics. The latter will be conducted using a combination of PIV and PSP measurements. By achieving its objectives, TUC-TUC aims to contribute to a deeper understanding of rotor noise generation mechanisms and to provide a comprehensive experimental dataset for the development and validation of predictive methodologies.

## ACKNOWLEDGEMENTS

The authors gratefully acknowledge Wouter Gregor, Stefan van t' Hof, and Lars Leenheer (TU Delft DEMO) for their support in engineering, designing, and manufacturing key components. The authors also express gratitude to BerkelaarMRT for engineering design and assistance with the rotor rig/dynamic pitch system, MuTech for permitting modifications to their airfoil pitch system, and Bert Bruil (Elma Vortex BV) for help balancing TUC-TUC.

## REFERENCES

1. FAA.gov. Package delivery by drone (part 135) | federal aviation administration, 2023.
2. FAA. Unmanned aircraft system traffic management (utm) | federal aviation administration.
3. EASA.Europe.eu. Easy access rules for u-space (ir+amc/gm) | european union aviation safety agency.
4. EASA. Study on the societal acceptance of urban air mobility in europe. *Full Report, European Union Aviation Safety Agency (EASA)*, 2021.
5. D. B. Hanson. Influence of propeller design parameters on far-field harmonic noise in forward flight. *AIAA Journal*, Vol. 18(No. 11):1313–1319, 11 1980.
6. F. Farassat. Derivation of formulations 1 and 1a of farassat. *NASA TM-2007-214853*, 2007.
7. H. Hubbard, B. Magliozzi, D. B. Hanson, and R. K. Amiet. Aeroacoustics of flight vehicles: Theory and practice, propeller and propfan noise, vol. 1. Technical report, NASA, 1991.
8. Lourenco Tercio Lima Pereira, Daniele Ragni, Gianluca Romani, and Damiano Casalino. *Accuracy of Tonal Noise Prediction of Propellers via Numerical Simulations and Experimental Campaigns*.
9. F. d. Monteiro, R. Merino-Martínez, and L. T. Lima Pereira. Psychoacoustic evaluation of an array of distributed propellers under synchrophasing operation. In *30th AIAA/CEAS Aeroacoustics Conference*, 2024.
10. A. Piccolo, R. Zamponi, F. Avallone, and D. Ragni. Towards a novel physics-based correction to amiet's theory for inflow-turbulence noise prediction. In *30th AIAA/CEAS Aeroacoustics Conference*, 2024.
11. K. Disotell, T. Juliano, D. Peng, J. Gregory, J. Crafton, and N. Komerath. Unsteady pressure sensitive paint measurements on rotors in forward flight. In *AIAA 28th Aerodynamic Measurement Technology, Ground Testing, and Flight Testing Conference*, 6 2012.
12. A. Weiss, R. Geisler, T. Schwermer, D. Yorita, U. Henne, C. Klein, and M. Raffel. Single-shot pressure-sensitive paint lifetime measurements on fast rotating blades using an optimized double-shutter technique. *Experiments in Fluids*, 58:1–20, 2017.
13. D. Yorita, K. Asai, C. Klein, U. Henne, and S Schaber. Transition detection on rotating propeller blades by means of temperature sensitive paint. *50th AIAA Aerospace Sciences Meeting including the New Horizons Forum and Aerospace Exposition*, 1 2012.
14. R. Merino-Martínez, A. Rubio Carpio, L. T. Lima Pereira, S. van Herk, F. Avallone, D. Ragni, and M. Kotsonis. Aeroacoustic design and characterization of the 3d-printed, open-jet, anechoic wind tunnel of delft university of technology. *Applied Acoustics*, Vol. 170:107504, 2020.
15. K. L. Wadlin, R. E. Fontana, and C. L. Shuford. *The Effect of End Plate, End Struts, and Depth of Submergence on the Characteristics of a Hydrofoil*. NACA-RM-L51B13, 1951.
16. Leishman G. J. *Principles of Helicopter Aerodynamics*. Cambridge University Press, 2006.
17. Donald W Kurtz and JE Marte. A review of aerodynamic noise from propellers, rotors, and lift fans. 1970.
18. Markus Raffel, Christian E. Willert, F. Scarano, Christian J. Kahler, Steven T. Wereley, and Jurgen Kompenhans. *Particle image velocimetry: A practical guide*. Springer, 2018.